

THE CALIBRATION OF VIDEO CAMERAS FOR QUANTITATIVE MEASUREMENTS

Walter L. Snow
NASA Langley Research Center
Mail Stop 236
Hampton, VA 23681-0001, USA

Brooks A. Childers
NASA Langley Research Center
Mail Stop 236
Hampton, VA 23681-0001, USA

Mark R. Shortis
Department of Surveying and Land Information
The University of Melbourne
Parkville, Victoria 3052, AUSTRALIA

KEYWORDS

Calibration, CCD, Videometry, Close range, Model Deformation

ABSTRACT

Video is being used more and more as a quantitative measurement tool in field applications. This paper will discuss one viable approach for calibration of digitally rendered video sequences using analytical photogrammetry tools. Some practical consequences of using intermediate storage media such as video disk or super VHS tape will be discussed as will data pertaining to the extraction of irradiance information.

1. INTRODUCTION

The word television was coined more than 50 years ago and television permeates every nook and cranny of the globe yet only recently has the term videometrics entered the vocabulary. This has been partly due to the ready availability of image capture boards for PC's and workstations which relieve the tedium of conventional hardcopy image measurement. Another more insidious reason may be the rapid evolution of solid state CCD technology. The mental image one conjures of discrete, geometrically placed photosites is reinforced by the crisply indexed row and column pixel dumps on the computer screen. The euphoria is quickly dispelled when the user realizes that the Pythagorean theorem cannot be applied to the pixel units without first establishing the metric for the space.

This paper will describe several different recent applications of videometry at Langley Research Center by way of introducing the need for calibration. Close range photogrammetrists have developed an arsenal of robust analytical techniques over the past several decades for calibrating conventional cameras. These powerful techniques are working their way into the video arena with positive consequences. Due to these efforts quantitative triangulation schemes can be successfully applied to data acquired at video rates and post processed making it possible to study dynamic events quantitatively. A number of problems peculiar to video sensing will be discussed as will the burgeoning interest in extending the measurements to include radiometric estimates. A number of *digital* cameras are appearing in the marketplace which should lead to improved accuracies in the near future.

2. AEROSPACE EXAMPLES OF VIDEOMETRY

2.1 Model Deformation at NTF

The National Transonic Facility (NTF) is a cryogenically cooled, high pressure wind tunnel designed to test at full scale Reynolds numbers ($Re_{\#}$). The high dynamic pressures incurred to achieve high $Re_{\#}$ can result in significant model deformation. Video based model deformation schemes based on triangulation techniques have been under development for several years.^{1,2} A view from one of the video camera stations is shown in the figure 1.

The task of obtaining quantitative video measurements in the harsh environment of this facility has afforded many challenges which will not be addressed in this paper. Attention is drawn, however, to illumination and targeting considerations. High $Re_{\#}$ is concomitant with thin boundary layers. Model surfaces are highly polished thus precluding the attachment of high contrast (e.g. retro reflecting) targets usually associated with close range photogrammetry. In this case black ink markings were deemed suitable to avoid inducing transition from laminar to turbulent flow. The reader will appreciate the difficulty of discerning the first moments of the light patterns associated with these targets in the presence of glints and low contrast imagery. To complicate matters even further, the illumination conditions are constantly changing as the model is tested at various attitudes.

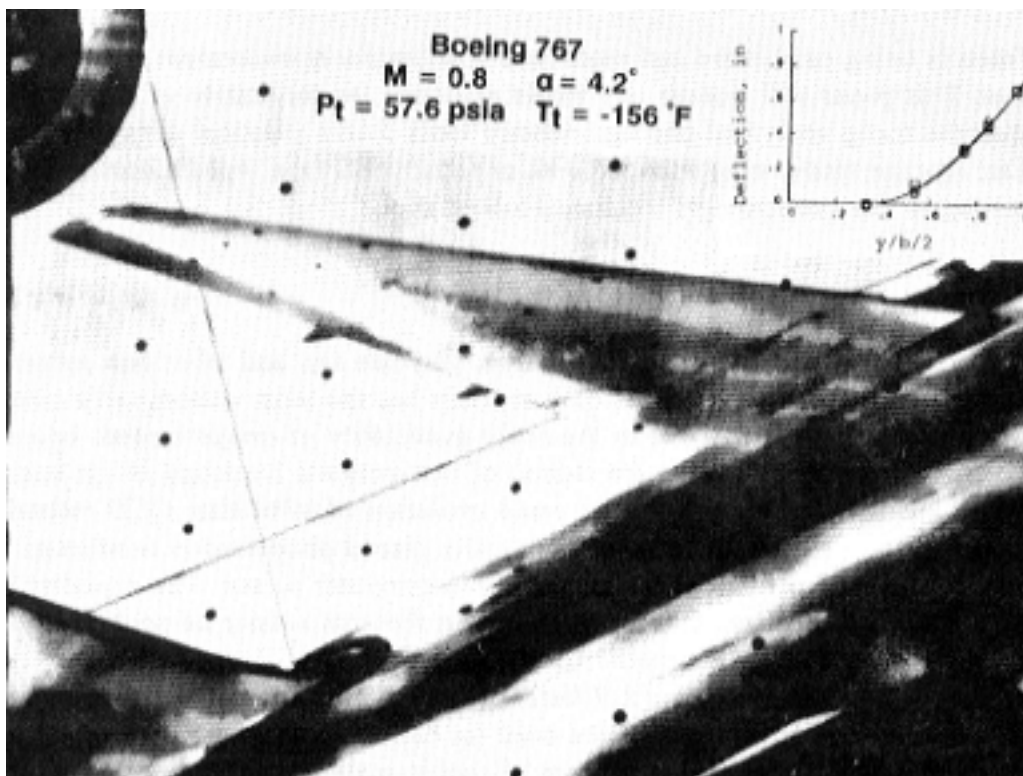


Figure 1. Video camera view of model in the National Transonic Facility.

2.2 Trailing vortex studies.

An inordinate amount of energy resides in the wing tip vortices generated by commercial transport aircraft. Not only do these flow structures incur drag penalties on the generating craft but also pose safety hazards for light trailing aircraft encountering the wake vortex which can lead to flow-induced upsets. The allowed minimum landing intervals at large airports are imposed primarily to

allow time for natural tip vortex dissipation. Landing time constraints often limit the throughput of large airports.

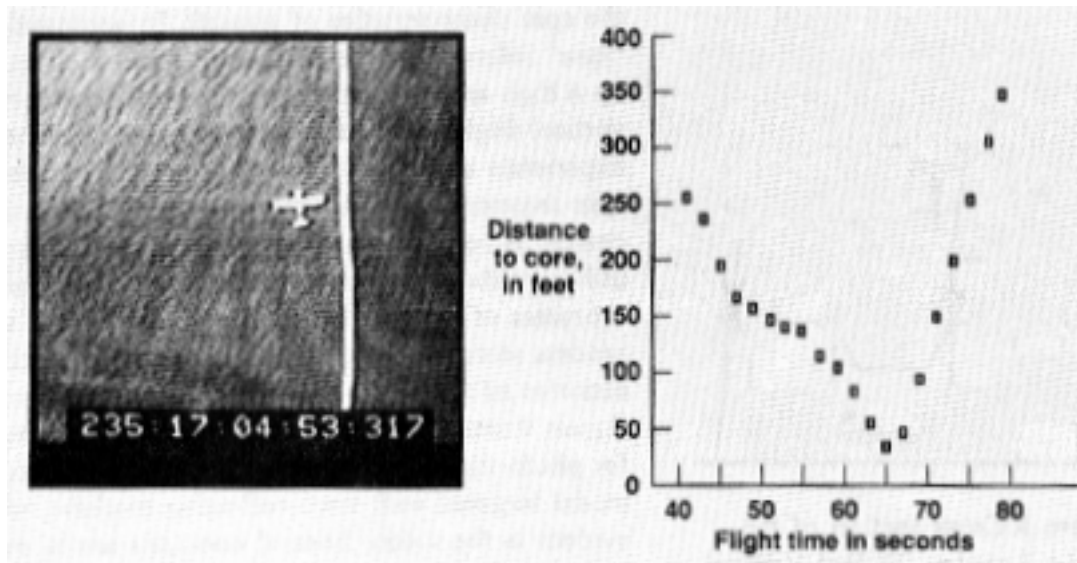


Figure 2. Video support of vortex interaction studies.

Since vortex flow is invisible, an effective warning system to detect the proximity of a vortex would be helpful for avoidance strategies. A feasibility study³ proposed an on-board wake avoidance system which uses state-of-the-art sensors (e.g. flow direction vanes, roll rate gyros, and accelerometers) to detect the proximity of a vortex. A series of tests were conducted to assess the feasibility of the approach. A crucial element of the proposed investigation was to provide an independent scheme to continuously monitor the encounter separation to correlate with the probe aircraft sensor data. A video based optical technique was used⁴. Smoke on the generating aircraft were used to demarcate the core. A finger-sized, down-looking camera was placed in the wingtip of an observer aircraft which flew a minimum of 500 feet above the instrumented probe plane. The probe plane pilot maintained a common altitude with the smoke trail so that the airplane could be used to scale the imagery. IRIG-B time code accurate to milliseconds was recorded to correlate image data with that of the probe sensors. Data was recorded to Super VHS tape and post processed. The camera was equipped with an 8mm focal length lens to provide an adequate footprint and thus introduced considerable distortion which had to be removed with calibration. The associated graphic shows a view from a typical video field as well as a synopsis of reduced data.

This example was chosen to represent a constrained, single camera problem which entailed considerable distortion, required miniature cameras, time encoded data, and a large data storage capability. Post processing of stored video was acceptable for this project.

2.3 Spin tunnel six-degree-of-freedom measurements.

Since WWII, the NASA Langley 20-Foot Vertical Spin Tunnel has been used to study the spin characteristics of aircraft. In aeronautics, “spin refers to an out-of-control motion characterized by a high angle of attack, high yaw rate, and near-vertical flight path. Engineers with broad testing experience used analysis of photographs to predict the spin recovery characteristics of models in the test stream. A recent report⁵ describes current efforts to utilize calibrated video cameras to provide real time estimates of the spin rate and pitch angle and to post process stored video data to recover detailed time histories of the position, pitch, roll, and yaw variables.

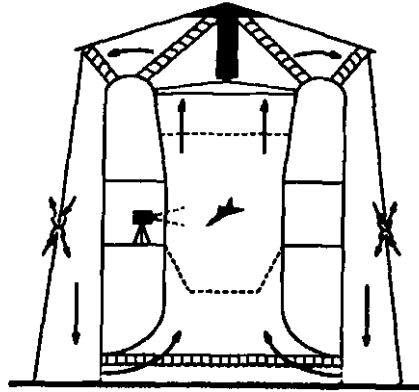


Figure 3. Cross section of the NASA Langley 20-foot Vertical Spin Tunnel.



Figure 4. View from one triangulation camera in the spin tunnel.

Figure 4 shows the view from one video camera used for photo-triangulation. The inset shows a typical model targeted with retro-reflective markers which are evident in the video. Several concerns are in evidence. The vertical streaking associated with bright spots are due to the frame transfer architecture of the Pulnix camera. The video is electronically shuttered to freeze the motion. What appears to be a dark background would be highly overexposed using conventional exposure times due to banks of flood lamps used to illuminate the test section. One bank of lamps is visible on the left hand side of the photo. Since streaks are artifacts of the image transfer and not relevant to the event being studied they only tend to bias the gray level centroids which constitute the data. The cameras will be replaced with electronically shuttered interline transfer cameras for future tests to avoid the streaking. Notice also that the light-stripe retro used for the real time Model Space Positioning System [MSPS] described in the reference is merged with the nose target.

A mosaic view from the triangulation cameras is shown in figure 5. The matching time codes are superimposed for illustration. Time code display would be suppressed for data manipulation. The model occupies only a small portion of the image and can leave the field of view as well. This example represents one of the tougher videometry problems. Camera coverage must be chosen to encompass a very large test volume and the measurements must be made on a very small segment of the image. In photogrammetry one tries to have the test object fill the camera frame. The test object roams even the far edges of the frame where distortions are large. Shuttered cameras must be used and there are contrasting lighting requirements. The volume of data is large and the so-called pixel flow can be tens of pixels per field so that identification of targets from interval to interval is difficult without operator intervention. The large amount of data, typically 10 Mbytes/second/channel, requires intermediate storage media which tend to degrade accuracy also.



Figure 5. Simultaneous fields for spin tunnel phototriangulation.

2.4 Leading edge vortex studies.

As demand for higher speeds and maneuverability has increased over the years for both fighter aircraft and missile development, the designer has been forced to modify his strict adherence to attached flow.⁶ Flow separation has historically been equated with loss of lift, increased drag and often loss of control. Typical fighters achieve maximum lift at 25 to 35 degrees angle-of-attack (AOA) and can experience pitch overshoots of twice that magnitude during aggressive maneuvering. At these incidence angles, detached flow is virtually guaranteed.

Significant increases in maximum lift and drag reductions can be obtained by controlling the leading edge vortices which form, to favorably interact with the flow over the main wing surfaces, resulting in improved maneuvering performance without incurring severe cruise performance

penalties. Judiciously placed structural modifications such as leading-edge extensions (LEXs) are sometimes used to generate vortex flow which would otherwise not exist.

Experimentalists are actively studying ways to characterize and predict the location and attributes of vortex flow both in flight^{7,8} and in ground based tests.⁹ Typically, vortex structure is visualized by introducing scattering centers into the flow. The flow is trans-illuminated with a narrow sheet of light. The presence or absence of scatterers which have been redistributed by the swirling fluid demarcate the vortex structure. Figure 6 was constructed using data from the Langley Research Center Basic Aerodynamic Research Tunnel (BART) of flow over a delta wing at high angle of attack. The BART is a facility dedicated to code validation. The figure depicts a synthesis of data obtained from various light sheet stations. The nearside patterns were obtained from experimental images and the starboard results are from computational fluid dynamic calculations for the same conditions.

This example was chosen to represent the more demanding photo interpretation tasks which will become more prevalent in the future. While targeted videogrammetry is susceptible to lighting as indicated in section 2.1, the perceived image plane irradiance in this case depends on physical properties inextricably bound to the physics of the problem. It is not clear, for example, that the first moment of the irradiance pattern characterizes the vortex core. The Mie scattering results are highly dependent on particle density and distribution, dielectric properties of the scatterer, size distribution and thermodynamics influencing the formation and depletion of particles.

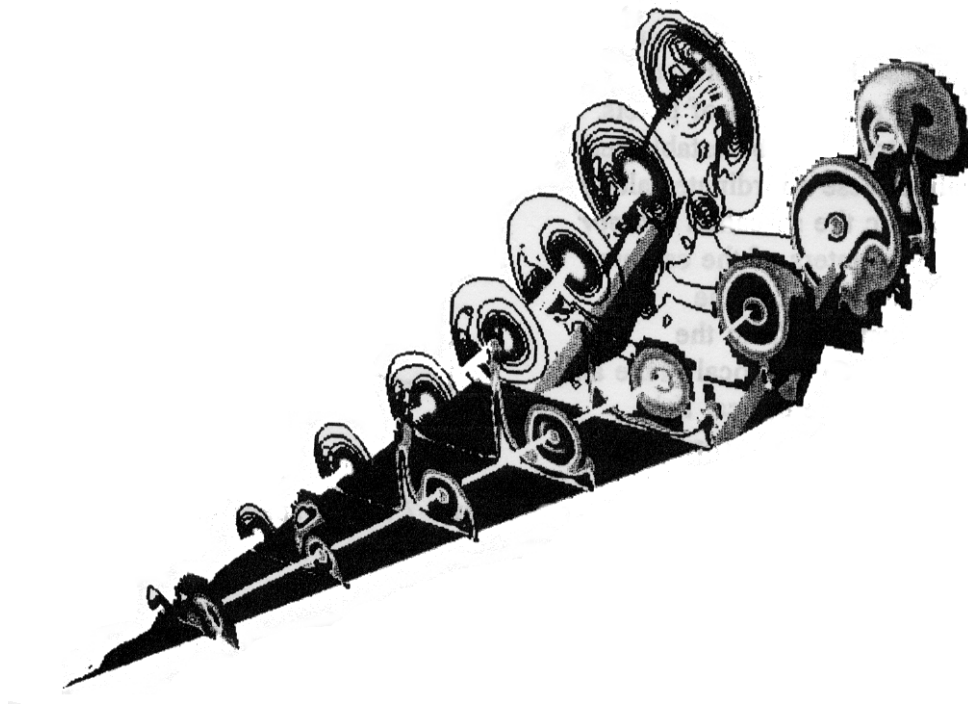


Figure 6. BART delta wing vortex-fin interaction studies.

3. CAMERA CALIBRATION

3.1 Calibration defined

Calibration is used here in a limited sense and deals only with the removal of optical and electronic distortions which subvert the collineation of image, object, and perspective centers when

conventional video cameras are used for mensuration. Only when this is done can the power of Euclidian geometry be used to infer object space information from image space measurements. The calibration procedures described here rely on accurate measurement of the first moments of blobs of relative irradiance on the focal plane and this is much less demanding than the inference of radiometric signatures as is required in astronomy, for example.

Photogrammetric triangulation is based on the collineation of image, object (P) and perspective center (O) points as suggested in figure 7. Even in this idealized “pinhole” camera geometry one must establish an appropriate image plane coordinate system. For video, an arbitrary origin might be defined by the intersection of the central row and column of pixels. An appropriate metric must be established to dimensionalize these coordinates along with x_p , y_p , and c the so-called *interior orientation* parameters of the camera. The principal distance c is the perpendicular distance from the perspective center to the focal plane and the point at which the optical axis penetrates the image plane (principal point) is designated by x_p , y_p . The principal point introduces the physics of the problem and is, for example, the center of symmetry for many optical distortions.

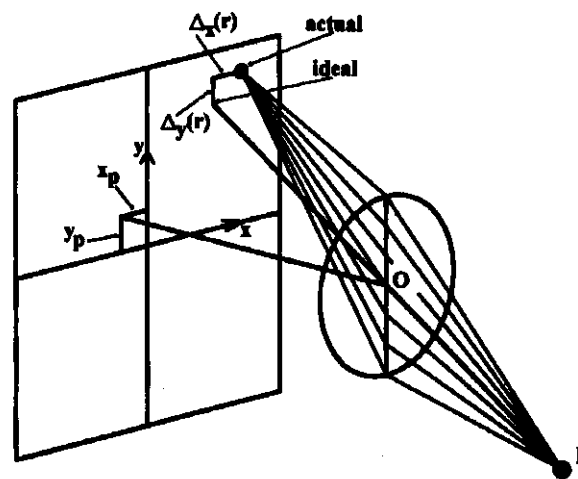


Figure 7. Image space geometry.

3.2 Common misconceptions

The well deserved reputation of scientific CCD cameras for being highly linear is often falsely assumed to apply to their inexpensive commercial relatives. The nonlinearity issue will be briefly addressed later. For videometry measurements, only the first moments of relative irradiance blobs spanning many pixels are of interest and the penalty incurred by mild nonlinearity and low gray scale dynamic range has not been adequately assessed.

Another widely held erroneous assumption is that the discrete nature of the solid state sensor (sels) translates itself unambiguously into the picture elements (pels or pixels) of the PC world. This is unambiguous for slow scan scientific solid state (CCD, CID) cameras. The typical commercial camera has electronic circuitry in the head which generates an analog composite sync waveform suitable for display on a standard monitor. This is suggested in figure 8. The analog output would not reflect the sel spacing of the parent array. Typically, a frame grabber dc restores the analog waveform and resamples it with A/D circuitry which establishes the pixel space geometry depicted in the center of the figure. Sample spacing depends on the pixel clock reference. Several manufacturers provide the actual sd clocking signal which ensures that the samples are acquired at the same rate that they are dumped onto the analog train. The decision to begin digitizing, however,

is based on some arbitrarily chosen delay from say the rising edge of horizontal sync tip as shown in the figure.

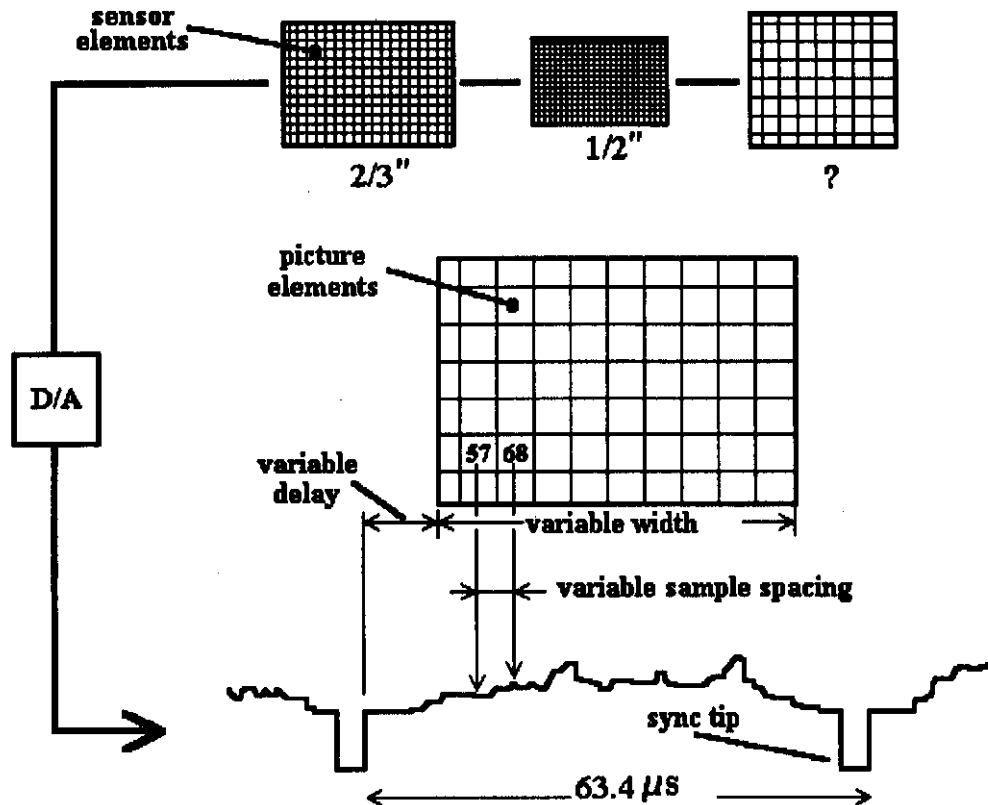


Figure 8. Cartoon relating sensor elements to picture elements' via waveform sampling.

Obviously, the pixel coordinate system can shift horizontally by an arbitrary amount with respect to the parent sel landscape. This latitude is pernicious in applications requiring frame registration and would be avoided with slow scan devices where a (relocatable binary) memory address is uniquely associated with a sensor element.

3.3 State-of-the-art approach.

To recover the "idealized" image points one must account for image plane displacements labelled by Δ_x and Δ_y in figure 7 of section 3.1. Fortunately, the photogrammetry community has had four decades of analytical experience in establishing these corrections¹⁰. State of the art procedures allow image plane distortions to be corrected to residual uncertainties on the order of one pm. It is especially significant to achieve this accuracy for the small format electronic focal plane sensors.

The merits and demerits of mathematical approaches to calibration are to be found in the specialized literature. The pitfalls of over or under parametrizing nonlinear models with highly correlated variables will be appreciated by researchers from many disciplines. We have found a "test range" approach to calibration rather easy to use and quite reliable. Our "test range" is pictured in Figure 9. Several components are evident including a plumb line panel (tensioned nylon cords), independently measured target plates, a video waveform scope, a TV signal generator, tape recorders, and an AT-class personal computer.

The idea is to acquire a series of images of a known object from different perspective vantage points and to iteratively adjust distortion parameters, interior orientation, and exterior orientation until a self consistent set of image and object points is obtained. Powerful software programs are becoming

available to accomplish this rather burdensome task. This work uses Close Range Multi-station Photogrammetric Adjustment (CRAMPA)¹¹ which is actually a suite of programs written in the C language and portable to a number of different computers. The many features of this versatile package are noted in the product literature.

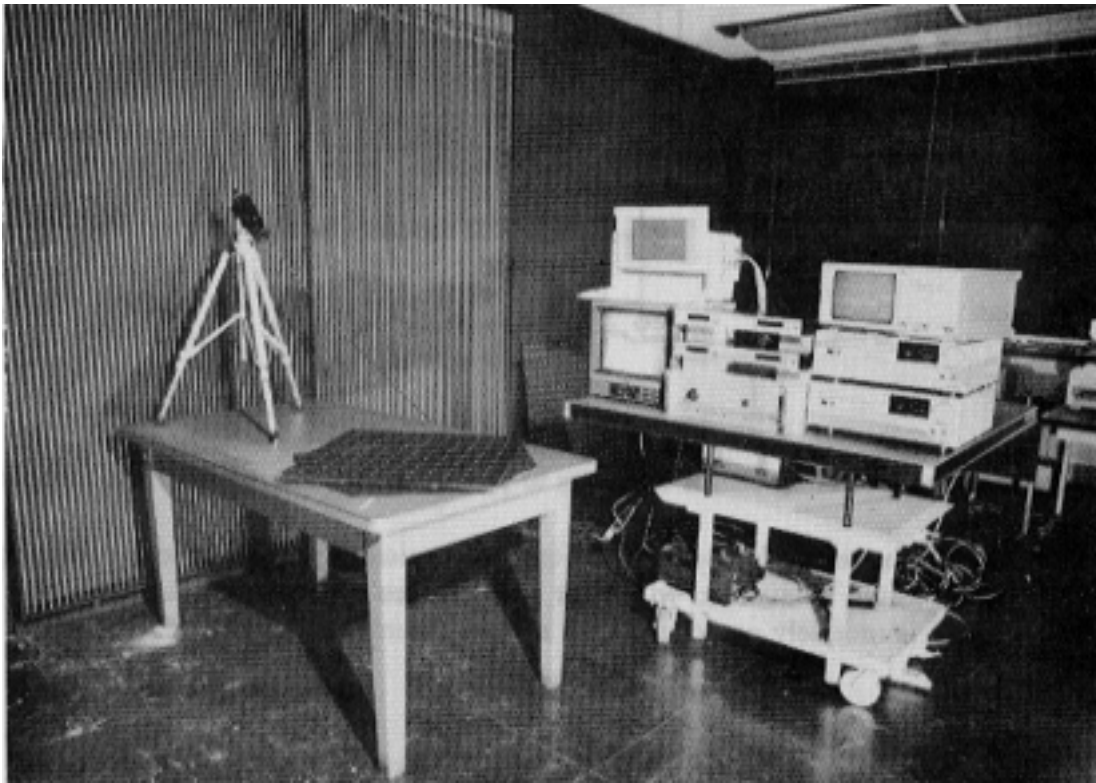


Figure 9. Laboratory test range.

Experience has shown that most video cameras are quite well characterized by including one or more radial distortion terms (K_i), two decentering coefficients (P_1 , P_2) and affinity terms (a_1 , a_2) to accommodate non-orthogonality and scale of the sensor axes. Distortion is reckoned with respect to the principal point (see figure 7) and radius is defined by equation (1). The governing equations are:

$$r^2 = (x - x_p)^2 + (y - y_p)^2 = x^2 + y^2 \quad (1)$$

$$\Delta_x(r) = x (K_1 r^2 + K_2 r^4 + K_3 r^6) + P_1 (r^2 + 2x^2) + 2P_2 xy \quad (2)$$

$$\Delta_y(r) = y (K_1 r^2 + K_2 r^4 + K_3 r^6) + 2P_1 xy + P_2 (r^2 + 2y^2) + a_1 x + a_2 y \quad (3)$$

The plumb line data is based upon the fact that straight lines in object space would project to straight lines on the image plane for an ideal camera. Figure 10 is a mosaic view of the plumb line set with four different camera rolls. One important feature is that the entire image plane is covered. This is awkward to achieve for a complete set of targets due to the aspect ratio of conventional television. The plumb line analysis is quite suitable for recovery of the K_1 and P_1 terms in the equations above. Similarly, the target plate is viewed from different directions with camera roll incorporated to help de-correlate the interior orientation parameters. A single view of a test plate is shown in figure 11. Usually 8 to 16 views are used. Using these strategies, one recovers a reliable set of photogrammetric calibration parameters and some useful statistical figures of merit as well.

Significantly, the system calibration can also incorporate alternate recording media (tape, disk, etc...).

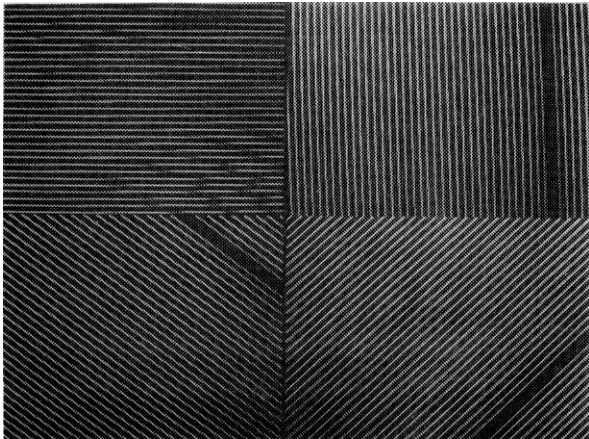


Figure 10. Mosaic of plumb line images.

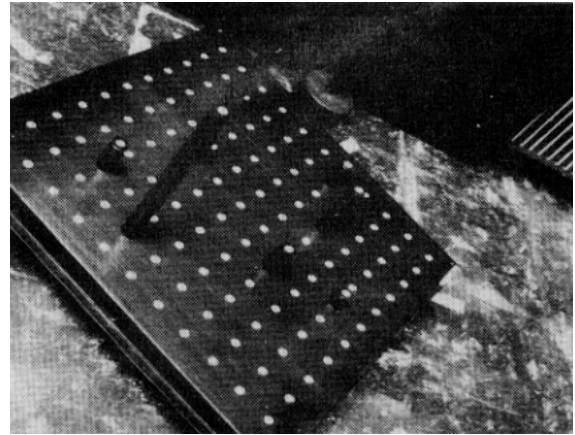


Figure 11. Single view of calibration plate.

3.4 Low budget option

Given the small size of electronic sensors vis a vis their film counterparts, one is advised to utilize state of the art techniques for calibration to optimize proportional accuracy on the focal plane. The approach described in the previous subsection can accommodate distortions introduced throughout the entire data acquisition chain including the effects of storage media (video disk, tape recorder), windows, etc. This section describes a zeroth order alternative when neither sophisticated software nor precise optical shop techniques are available. Experience has shown that x_p , y_p are difficult to determine without powerful analytical techniques and in the absence of reliable estimates should probably be set to zero. Furthermore, the predominant optical distortion is usually dominated by the K_1 term. The assignment of a metric on each axis [pm/pixel] is significant and should be determined.

3.4.1 Affinity corrections.

Ultimately, measurements in pixel units must be converted to physical units using horizontal (S_h) and vertical (S_v) scale factors. Reasonable estimates for these factors are sometimes available from the specification sheets for solid state cameras but never in the case of analog devices. Assumed choices should be verified along with implied orthogonality of pixel axes. The procedure used in videometry is to make measurements of image features in raw pixel coordinates, convert to physical units and refine or correct for distortions using an appropriate model. For the *affine set* represented by equations (2) and (3), the affinity is arbitrarily associated with y . With the signs adopted

$$r_{\text{refined}} = r_{\text{observed}} - \Delta(r)$$

The geometric significance of a_1 and a_2 can be gleaned by assuming x_p , y_p , $\{K_i\}$, and $\{P_i\}$ are zero. Then

$$x_{\text{refined}} = x_{\text{observed}}$$

and

$$y_{\text{refined}} = (1 - a_2) y_{\text{observed}} - a_1 x_{\text{observed}}$$

Points $(0,y)$ and $(x,0)$ on the dashed pixel axes map to the refined axes (solid) as $(0, (1 - a_2)y)$ and $(x, -a_1x)$. The non-orthogonality is manifest through $\tan^{-1}(a_1)$ and the y axis scaled by $(1 - a_2)$.

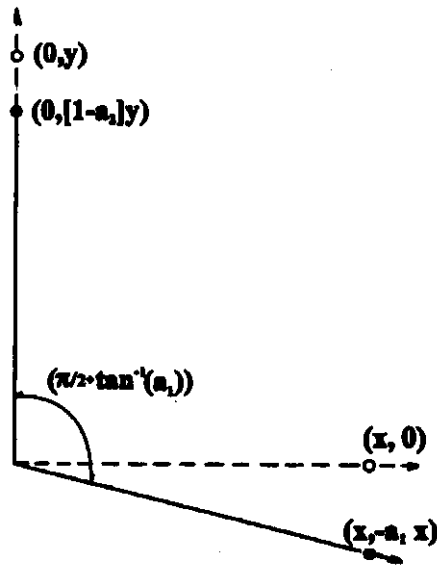


Figure 12. Sketch to interpret a_1 and a_2 .

To establish S_h and S_v , a simple targeted mirror has been found to be useful. A small circular decal is placed at the intersection of two orthogonal scale lines L_x and L_y roughly proportional to the 4:3 aspect ratio of the television sensor. The camera is adjusted with respect to the mirror until the decal is concentric with the camera's view of its own lens in reflection, thus ensuring that object and image planes are parallel and displaced axially so that the images span the screen dimensions. Figure 13 depicts the experimental arrangement. Let s denote the image scale, L_x and L_y object dimensions and l_x and l_y the corresponding image dimensions in pixel units and S'_h and S'_v , the assumed axial scale factors.

$$l_x \text{ [px]} S'_h \text{ [\mu m/px]} = s[.] L_x \text{ [mm]}$$

$$l_y \text{ [px]} S'_v \text{ [\mu m/px]} (1 - a_2) = s[.] L_y \text{ [mm]}$$

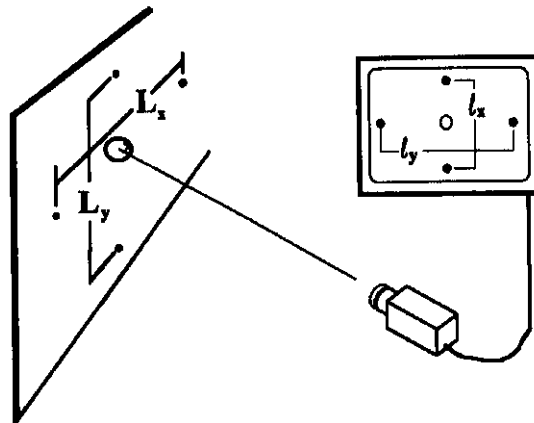


Figure 13. Inexpensive test rig to establish scale.

Dividing the first equation by the second to eliminate $s[.]$ and rearranging slightly:

$$\frac{S'_h}{S'_v(1-a_2)} = \frac{L_x I_y}{L_y I_x}$$

Then a_2 can be ascertained for the model as

$$a_2 = 1 - \frac{S'_h L_y I_x}{S'_v L_x I_y}$$

or alternatively a_2 can be made zero by letting $S_h = S'_h$ and $S_v = S'_v(1-a_2)$.

3.4.2 Radial distortion estimate

In many cases, the optical distortion can be adequately characterized by the first radial coefficient K_1 . When this is true, then with the caveat that x_p, y_p are zero, K_1 can be estimated using observations on a single straight line. The cubic nature of this distortion is noted in figure 14 where the distortion of a rectangle ($K_1 = 0$) is shown for cases of negative K_1 (so called barrel distortion), and positive K_1 (pin cushion). For barrel distortion, the ideal points are drawn toward the center so that a line looks concave.

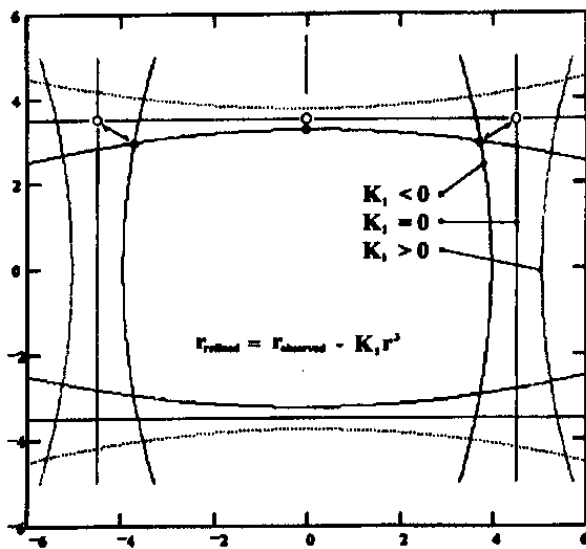


Figure 14. Sketch to describe first radial distortion coefficient.

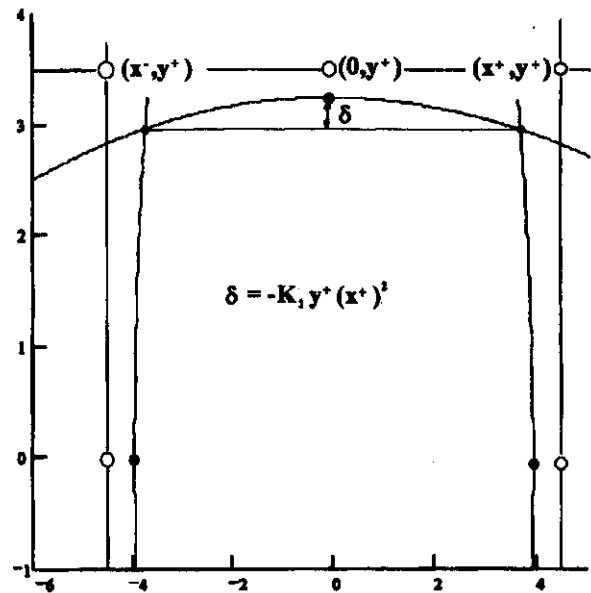


Figure 15. Sketch depicting the relationship of the sagitta to radial distortion.

For either sign, K_1 can be estimated by measuring the sagitta^a of the distorted line. Any line can be chosen but the longer it is and the further it is from the origin, the better. For concreteness consider the top horizontal line shown in figure 15. Points designated by open circles transform to the solid counterparts. Equation (3) can be used to establish δ viz.,

$$\begin{aligned} \delta &= \Delta_y(x^+_{\text{refined}}, y^+_{\text{refined}}) - \Delta_y(0, y^+_{\text{refined}}) \\ &= K_1 y^+_{\text{refined}} (x^+_{\text{refined}})^2 \\ &\approx K_1 y^+_{\text{observed}} (x^+_{\text{observed}})^2 \end{aligned}$$

^a Sagitta: distance between the midpoint of an arc and the midpoint of its chord.

where the last approximation makes use of the fact that the distortions are orders of magnitude less than the coordinates themselves. Lest the reader be troubled by the asymmetric way the radial distortion appears in Cartesian components they will note that

$$\Delta^2 = \Delta_x^2 + \Delta_y^2 = (x^2 + y^2) K_1^2 r^4 = K_1^2 r^6$$

therefore, $\Delta = K_1 r^3$ as expected. The independent Cartesian components are more convenient when dealing with image plane coordinates.

The following table was prepared to compare the results using a powerful analytical photogrammetry analysis code with the zeroth order treatment for a finger sized camera and an assortment of lenses. The proportional accuracy Σ_8 is a relative index used by close range photogrammetrists to characterize a camera used in strong triangulation configurations. The subscript denotes the number of independent views acquired by the single camera from different vantage points. If a camera has a proportional accuracy of 10^4 then if an object having dimension of 10 inches fills the camera frame it should be measurable to 0.001 inches. The frame grabber in this case digitized 752 x 480 pixels and the sensor active area is listed as 6.39 mm x 4.88 mm. The approximate scale factors were estimated to be $6.39/752 \approx 8.5 \mu\text{m}$ for S_h and $4.88/480 \approx 10 \mu\text{m}$ as noted in the table heading. Camera calibration attempts to improve on these estimates if the device is to be used for measurement tasks.

Elmo Model EM-102BW $S_h = 8.5 \mu\text{m}$, $S_v = 10.0 \mu\text{m}$								
	4mm		7.5mm		15mm		24mm	
	full	partial	full	partial	full	partial	full	partial
xp[mm]	0.2353	-	0.3315	-	0.1218	-	0.5065	-
yp[mm]	0.1876	-	0.1040	-	0.0322	-	0.1372	-
c[mm]	4.0604	3.9803	7.7579	7.5625	15.2611	15.2918	24.5744	24.5077
K_1 [mm ⁻²]	-1.6355(-2)	-1.5255(-2)	-9.0565(-3)	-11.447(-3)	8.2107(-4)	8.8959(-4)	-2.6602(-4)	-1.966(-4)
K_2 [mm ⁻⁴]	4.0790(-4)	-	-1.3707(-4)	-	1.0477(-5)	-	-7.8328(-6)	-
K_3 [mm ⁻⁶]	-6.6709(-6)	-	2.2973(-5)	-	0.	-	0.	-
P_1 [mm ⁻¹]	-6.1090(-5)	-	-1.1088(-4)	-	-3.8716(-4)	-	3.5326(-5)	-
P_2 [mm ⁻¹]	1.2046(-4)	-	-3.5575(-5)	-	-1.7403(-4)	-	1.0125(-4)	-
a_1	-9.9876(-5)	-	2.5797(-4)	-	6.6557(-4)	-	-7.7118(-4)	-
a_2	1.7289(-4)	6.0024(-2)	-2.1677(-4)	4.5621(-2)	-3.4993(-4)	-3.0704(-3)	-2.9601(-4)	3.6535(-3)
Σ_8	10600	600	15200	1300	15500	4300	14800	9100

This particular camera had very little affinity correction as evidenced by the full treatment. The partial treatment suggested otherwise especially in cases where large radial distortion was present. No iteration of the a_2 and K_1 estimates were done for this table. As might be expected the proportional accuracy is adversely affected in all cases whereas the full treatment accommodates even the severe distortion of the shortest focal length lens. Also not evident is the statistical significance and correlation information available from the analytical treatment or the ability to use much more elaborate error modeling schemes.

3.5 Challenging modeling problems

3.5.1 Calibration of individual fields

To obtain acceptable time resolution using commercial video cameras, individual fields are acquired and analyzed. Interlaced fields were adopted in the developmental stages of television to accommodate electronic bandwidth limitations as well as the peculiarities of the human visual system. Odd numbered rows of the sensor contain information obtained $\frac{1}{160}$ di of a second after the information retained in the even rows. When post-processed as individual fields, the analysis recognizes separate, renumbered images at one half the vertical resolution. For a typical frame grabber, the row correspondences might be:

FRAME₀ -----> EVEN₀
 FRAME₁ -----> ODD₀
 FRAME₂ -----> EVEN₁
 FRAME₃ -----> ODD₁
 FRAME₄₇₈ -----> EVEN₂₃₉
 FRAME₄₇₉ -----> ODD₂₃₉

In terms of the physical distortion model considered, one might expect the optical aberration and affinity corrections to be the same with perhaps a fractional pixel shift in the y_p , estimate. The principal point (x_p, y_p) is, of course, defined in terms of the total active area of the sensor. Based solely on the indexing conventions, the even field does not recognize the last row of active sensor elements while the odd field fails to recognize the top row. To test the y_0 shift hypothesis, a frame calibration was performed. The stored image files were then parsed into individual fields so that identical data were involved. Only the y_0 parameter was allowed to float in the field analysis to avoid redistributing error into unrelated parameters. The results are shown in the accompanying table:

field	both	even	odd
x_p [sel]	-3.0	-3.0	-3.0
y_p [sel]	18.5	18.3	18.9
c [mm]	12.6	12.6	12.6

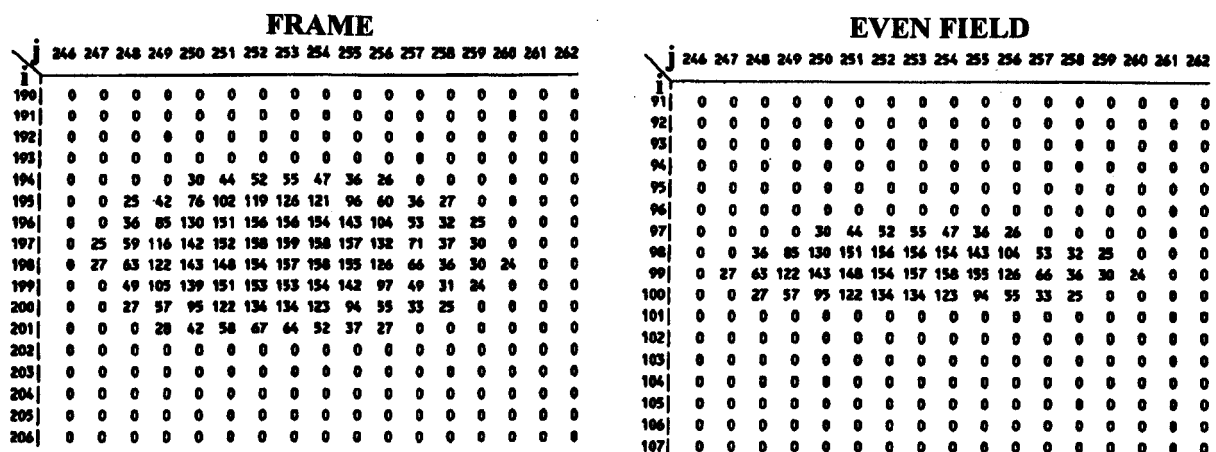


Figure 16. Pixel peek of a thresholded target image.

There is shifting in the appropriate direction, but not the simple ± 0.5 pixels. One potential source of discrepancy could be the numbering convention cited above. All target data is computed using simple gray level centroiding. If g_{ij} represents the gray-level of the ij^{th} pixel, then the centroid of a target image $\langle x \rangle, \langle y \rangle$ is computed as:

$$\langle x \rangle = \frac{1}{G} \sum_i \sum_j j g_{ij} \quad \langle y \rangle = \frac{1}{G} \sum_i \sum_j i g_{ij}$$

where

$$G = \sum_i \sum_j g_{ij}$$

and the sums range over the pixel dimensions of the local centroiding window. For this test, the computational algorithm in the CRAMPA suite was not modified to reflect the renumbering thus the row weighting might be slightly inappropriate.

An additional source of discrepancy could be the loss of information in the parsed fields. Figure 16 shows a particular target on one frame and its parsed even field counterpart. The renumbering is evident as well as the identical gray level values. It is well established² that more than four pixels should span the target if sub-pixel centroiding information is to be obtained. The worst case scenario is when a single pixel is 'illuminated' with uniform probability. Let W be the pixel dimension and $f(y) = 1/W$ be the uniform probability density. Then,

$$\langle y \rangle = \int_{-\frac{W}{2}}^{\frac{W}{2}} y f(y) dy = \frac{1}{W} \int_{-\frac{W}{2}}^{\frac{W}{2}} y dy = 0$$

and

$$\int (y - \langle y \rangle)^2 f(y) dy = \frac{1}{W} \int_{-\frac{W}{2}}^{\frac{W}{2}} y^2 dy = \frac{W^2}{12}$$

Therefore, the rms centroiding accuracy will roughly be one third of a pixel. Numerical experimenting with small targets showed up to one half pixel centroiding jitter depending on the row symmetry of the target. The strategy for calibration of individual fields is currently unresolved and is being further studied.

3.5.2 Window considerations

Measurements made on models in wind tunnels using digital photogrammetric techniques require the solution of a number of problems, not least of which is the camera calibration. Although lighting and environmental issues are often overriding factors, optimal accuracy within the wind tunnel cannot be obtained without an appropriate calibration. The technique most often used is to pre-calibrate the CCD camera in the laboratory, and then to hold the calibration fixed for use in wind tunnel measurements.

However, this strategy does not work when the wind tunnel environment requires glass ports to be interposed between the camera and the model test area. The introduction of an inclined plate of different refractive index than the surrounding air introduces an effective change in focal length and some well known distortions into the camera¹³. To detect the influence of a plane glass port on the performance of a digital camera system, an experiment was performed using a slow scan scientific CCD camera and a self calibration network. Fifteen camera stations in a conical array were used by rotating a test field plate while holding the camera fixed in position. This design was used deliberately to emulate what might be possible in a wind tunnel test situation. The test field plate

had been previously measured by an independent photogrammetric survey, and in this circumstance would be used as a known calibration fixture.

In the first instance the fifteen frames were taken without the glass plate in position in front of the lens. The target images were measured and the data reduced as a self calibration photogrammetric network. The glass plate was then introduced and the procedure repeated. The results of the network analyses are shown in the accompanying table.

Case	Plate	Calibration	RMS image plane residuals	Number of rejections
1	No	Free	0.55	12
2	Yes	Fixed from 1	3.19	41
3	Yes	Free	0.91	62
4	Yes	Free, extra parameters	0.82	35

The influence of the glass plate is clearly shown in the severe degradation apparent between cases 1 and 2 in the table. The RMS error at image scale^b is grossly inflated, as is the number of rejections^c of image measurements. The calibration derived from the no plate case is obviously inappropriate for the case with the plate. The conclusion that some extra modelling must be made is clear. In case 3 the calibration parameters for the camera are allowed to *float* and there is some improvement. The RMS error decreases, but the number of rejections increases. The RMS error decreases because the focal length, lens distortions and positions of the cameras all are adjusted to reduce the systematic errors in the network. The overall change to the focal length and range between the camera stations is approximately 2%, in coarse agreement with that predicted by analysis of the optics of the glass port. The characteristics of the lens distortions also changed, but to a lesser magnitude. The number of rejections increases because the smaller RMS allows images (perturbed by the systematic errors) to be rejected with greater statistical confidence. This allows better modelling, so the two effects are self-reinforcing to a certain extent.

In case 4 a full set of polynomial additional parameters was introduced to further reduce the systematic errors. The gain in fidelity here is only marginal. Losses in resolution due to the extra dispersive medium are not recoverable and simply add to the noise of the measurement system, so some overall degradation is unavoidable. This experiment shows that a calibration procedure can be used to recover some, but not all, of the systematic errors introduced by a plane glass port. The increase in noise caused by the port results in some degradation in all cases. The systematic component can only be entirely detected and modelled if a suitable change is made to the mathematical model used for the collinearity solution. Models of the influence of the multi-media light paths can be used very effectively¹⁴.

3.5.3 Recording media

The ideal acquisition system might be a scientific grade CCD camera operating at video rates which would associate each sensor element [sel] with a unique computer memory location within which would be stored a binary representation of its photo-generated charge. This choice is not yet available. Commercial solid state cameras deliver a video signal essentially indistinguishable from their analog predecessors. A/D converters in the PC key on the sync pulse information and re-sample this signal to provide a reasonable facsimile of the ideal system. The specialized literature abounds with examples of the merits and demerits of various synchronizing options. Seconds of video data can be acquired to memory but each video channel requires a computer front end and

^b A measure of the fidelity of the photogrammetric network.

^c Image which are deleted on the basis of over-large errors.

off-loading to disk is considerably slower. Real time disks using parallel bit streams can archive minutes of video but the cost is considerable and would be unacceptable in a multi-camera system.

Tape recording¹⁵ is a reasonably priced alternative, but extracting thousands of digital frames in a serial medium using start-and-stop techniques is tedious and deleterious to the data, not to mention the work involved in collating of independent stations. Video (analog) disks offer random access, can handle minutes of data and have excellent freeze-frame capabilities if data averaging of single frames is warranted. To avoid the expense of a video disk per data channel, the most viable option might be to record data to tape and then to use a single video disk recorder as an intermediate data buffer.

Tests were undertaken to estimate the accuracy loss incurred by the different storage options. The tests consisted of an 8 station laboratory calibration using plumb lines, a 121 target plate pictured in section 3.3, and CRAMPA data analysis. The following aliases are used to code the results:

Direct: Camera ---> PC
 Tape: Camera ---> Super VHS tape ---> PC
 Disk: Camera ---> Video disk ---> PC
 TapeToDisk: Camera ---> Super VHS tape ---> Video disk ---> PC

The tape results were acquired 'on the fly' to the frame grabber and were not 'freeze framed'. A Panasonic, model TQ-3038F optical disc recorder was used for these studies. The tape to disk recordings were buffered through a digital time base corrector as suggested by the manufacturer. The image plane residuals in both x and y dimensions are noted in the accompanying table along with the proportional accuracies.

	Direct	Tape	Disc	<Disc> ₈	Tape to Disc
σ_x [μm]	0.45	0.68	0.96	0.83	1.60
σ_y [μm]	0.39	0.68	0.62	0.51	1.11
Σ_8	31000	19200	16200	21100	9500

The optical disc signal was quite noisy as perceived on an oscilloscope or alternatively by watching pixel gray level fluctuations on the PC. The column labelled <Disc>₈ was obtained by utilizing 8 realizations of each still frame on the optical disk to see if averaging would help. There was obvious improvement and some statistical indicators that further modelling could improve the result further. The tape to disc results may have been corrupted with faulty time base correction and are the subject of further study.

4. PRACTICAL PROBLEMS

4.1 Synchronization and timing

Multi-station photogrammetric triangulation¹⁶ on static objects using large format metric cameras approach proportional accuracies of one part per million. Electronic cameras will not likely usurp these film based behemoths for large scale static measurements. For dynamic studies, video rate electronically shuttered cameras are ideally suited despite a proportional accuracy limitation due to sensor size. Timing and synchronization become significant issues. The Spin Tunnel application described in section 2.3 is an excellent example. The requirement for unique identification of

comparable events can be accomplished with vertical interval time code (VITC) as described by Snow et. al.⁵ Time code is visible in figures 4 and 5.

While it is possible to daisy chain the synchronization of cameras in master/slave fashion, a common distributed sync generator is preferable. Electronically shuttered cameras are becoming increasingly available and are essential to *freezing* the motion and avoiding image smear for rapidly changing scenes. These devices bias the collection of charge for fractions of a field time [16.7ms]. The time within the field in which the shuttering occurs is not usually provided by the manufacturer. It is essential to provide both horizontal and vertical synch to the cameras to ensure that exposures are in the same relative position within the field time. A technique found useful to verify proper timing is to observe a rapidly rotating targeted disk against a ruled background while recording time coded fields to tape. If the targets appear in the same relative position on correspondingly labelled fields, then correct timing is assured.

4.2 Targeting and lighting

The inference of the XYZ position of a target in space using photogrammetry presumes that its image is precisely located in at least two disparate images. Anyone who has attempted to place a measurement reticle on a low contrast, irregular image will appreciate the subjective nature of the problem. Trained photogrammetrists accordingly arrange for symmetric, high contrast targets on the object to be measured. Unfortunately, in field applications, this is not always possible and some criterion is established for determining the image location under less than ideal circumstances. The target image location is determined using some functional of the relative irradiance on the image plane. One popular choice is to use the grey level *center of mass* of the image as defined in section 3.5.1.

Obviously, only gray level due to the presence of the target should be included, otherwise the moment will be biased. Subsequent use of the incorrect image location will translate into an incorrect object space location. Typically some thresholding strategy is invoked to remove spurious background signal. To demonstrate the problem Trinder's strategy¹⁷ will be used on an admittedly artificial test case. The algorithm determines the threshold to be $(\text{mm pixel value} + \text{mean pixel value})/2$ for the pixels in the thresholding window. Gray level values below the threshold are set to zero and the threshold value subtracted otherwise. The experimental set up is as shown in Figure 17.

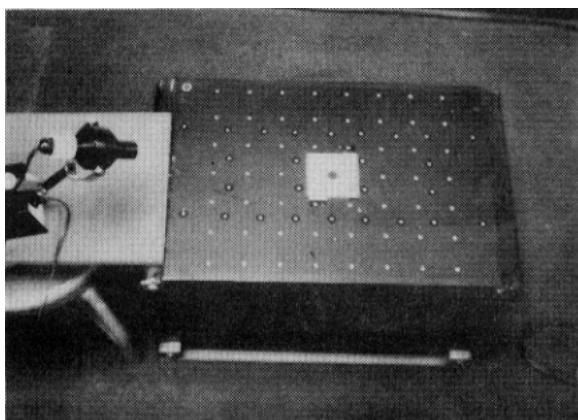


Figure 17. Setup for light bias experiment.

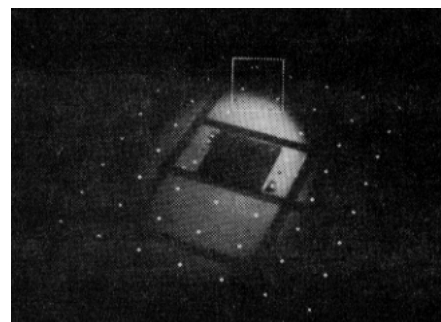


Figure 18. Irradiance pattern for light bias experiment.

The test object is essentially a flat plate with both retro-reflective and painted targets. The analysis was done for the 54 retro targets only since they had been measured very accurately independently. A microscope illuminator was used to cast a concentrated pattern of light on the object to reduce the contrast of the targets. By independently adjusting the current to the illuminator and the ring light

used to enhance the retro reflectors, the target contrast could be arbitrarily changed. Figure 18 shows a captured irradiance pattern. The retro-reflective targets are clearly evident even in the regions of high background lighting. In some cases the peak retro gray level was 160 superimposed on an average background field of 90. Figure 19 shows irradiance contours for the region demarcated by the box in figure 18. The contour interval is 22 gray levels. With the bias illumination removed the corresponding iso contours are shown in figure 20 [contour interval 19].

The latter constitute ideal targets from a photogrammetrists point of view. Trinder's algorithm was blindly used to perform the centroiding and the results used for two camera triangulation using a companion image. Camera resections were performed using only the four corner points which were not corrupted by additional lighting. Predicted answers were compared with the known values and the absolute Z discrepancies plotted in Figure 21. The dashed lines correspond to negative values and the solid to points predicted to be above the plane. *Induced* distortions of over 100 mils are in evidence especially in regions of strong gradients. When an appropriate threshold was set, *all* of the discrepancies were within 10 mils or so as shown in the non biased regions. One suitable scheme involved subtracting the max border + 5 gray levels and another by fitting the frame of the centroid window to a plane and subtracting the gray values in that plane. Even in the Trinder choice, a pixel peek of the processed target images indicated that there was residual background after correction so that a user might suspect problems. The point here is that there are choices to be made and that these choices can manifest themselves in very physical ways.

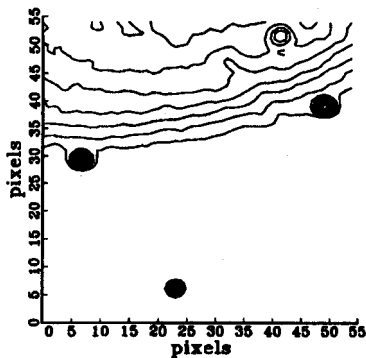


Figure 19. Irradiance contours for the box demarcated region of figure 18.

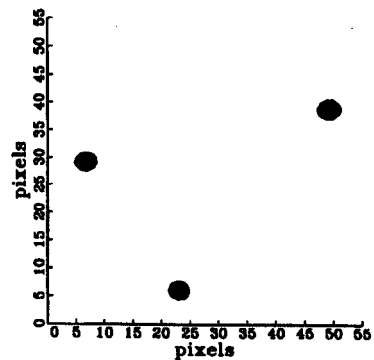


Figure 20. Isocontours using only retro-reflective markers without bias lighting.

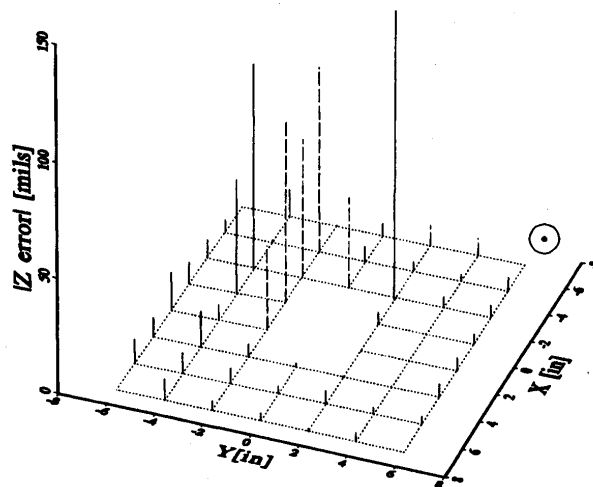


Figure 21 Errors induced by improperly thresholding biased image.

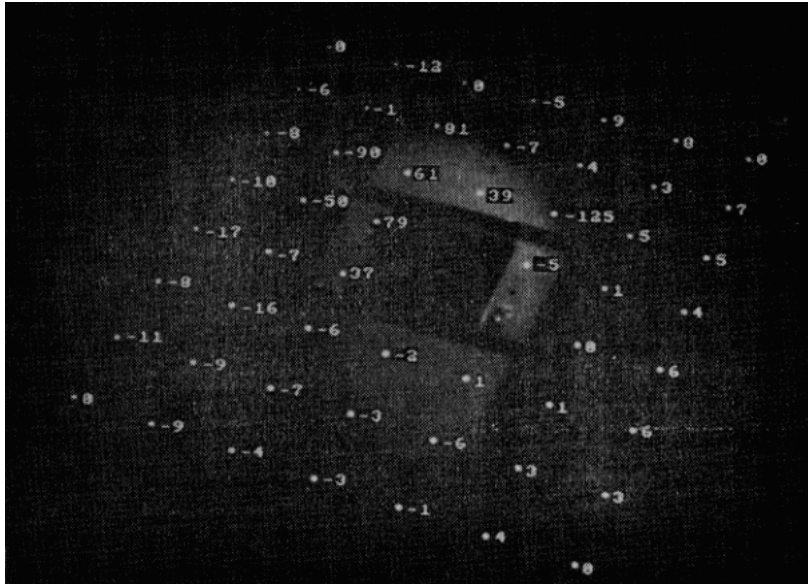


Figure 22 Bias errors in mils [0.001"] labelled on the raw image.

Figure 22 represents an image with the discrepancy in mils indicated next to each point. Largest problems occur in regions of severe gradients as might be expected. Unless each target image is laboriously edited, one never has the warm feeling derived from a contact method such as a coordinate measuring machine.

5. RADIOMETRIC CONSIDERATIONS

5.1 Linearity and uniformity

The much touted linearity of CCD detectors is often mistakenly assumed to apply to any camera with CCD in its designation. The linearity which can be better than 0.1% really applies to scientific CCD's which are driven by the requirements of the astronomical community. To achieve peak performance, research laboratories often rely on CCD test engineers who fine tune the clocking voltages and sources of noise to achieve optimum results. The best cameras are generally slow scan devices with sophisticated multi-sampled read out strategies. Commercially available cameras which sell for an order of magnitude less are not designed for radiometric work and in fact emphasis is on post sensor circuitry which provide the best visual impact on a television monitor.

Testing nonlinear behavior, especially for an area array is non trivial because it requires establishing the uniformity of an irradiance field which can be accurately attenuated. One usually resorts to a reasonable irradiance pattern and alters the exposure time since time intervals are easier to control. The nonlinear behavior of a high quality Pulnix TM-845 monochrome camera was established by time integrating the accumulated dark charge (lens cap on). The charge sensing read out gate cannot distinguish between an electron generated by a photon from one generated thermally. The charge build up is of course linear with time. The amplitude of the video waveform was measured using a waveform oscilloscope to eliminate possible nonlinear artifacts of the frame boards usually used to *measure* signal levels. Results are shown in figure 23 along with results from a slow scan scientific CCD using the same dark current integration strategy. The increased dynamic range of the scientific camera is also evident since it was Peltier cooled and designed for large electron well capacity.

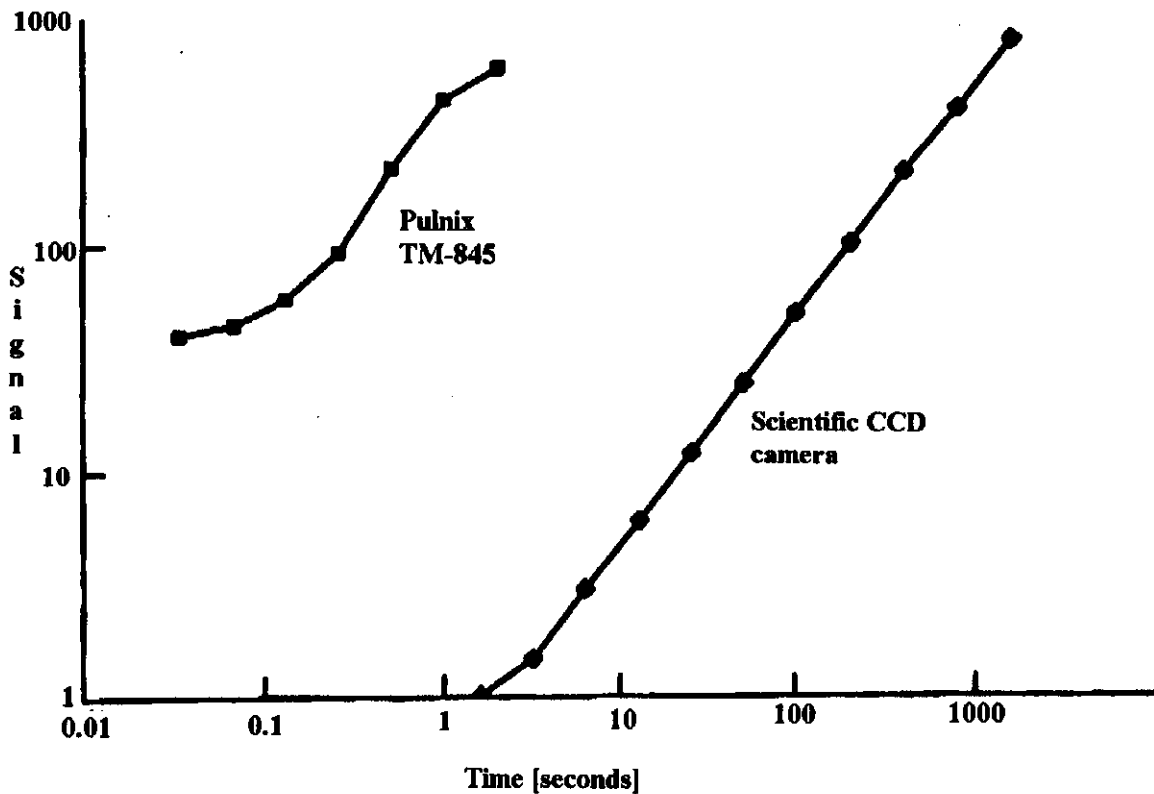


Figure 23. Comparison of linearity of commercial vs. scientific CCD cameras.

Time integrated field stores of the dark charge distribution were taken along with the quantitative waveform measurements. A startling variation was noted. Figure 24 shows a wire frame plot of two captures. The figure supports the rule-of-thumb that for typical CCD devices, dark charge under ambient conditions fills the potential well on the order of a second or so. New multi-pinned-phase architectures will improve this by an order of magnitude with some degradation in electron well capacity. The figure also shows that the dark current is irrelevant for 8 bit video data which refreshes the sensor every 0.016 seconds. No attempt was made to track down the reason for the variation but the camera is not marketed for time integrated irradiance measurements so it is not surprising that no attempt was made to uniformly heat sink the array. The center column is plotted for six exposure times in figure 25 to make the slope explicit.

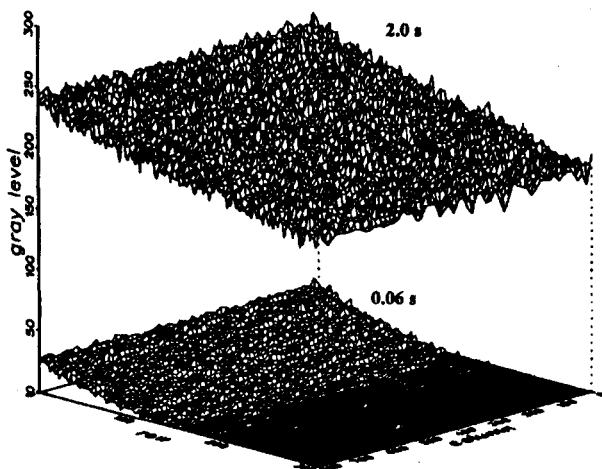


Figure 24. Dark charge distribution.

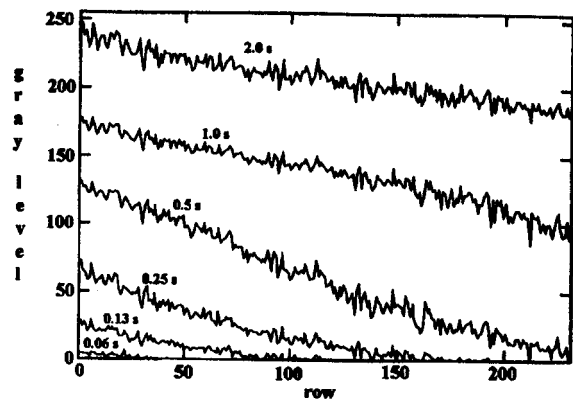


Figure 25. Column plot of dark charge buildup.

5.2 Irradiance studies

As noted in section 3.2, the PC integer matrix representation of relative irradiance belies the fact that commercial solid state cameras transduce the sensed charge into an analog waveform, usually in the camera head, with appropriate sync information and dc offsets to conform with standard monitors. The designer of the A/D board in the PC must establish a strategy for redigitizing this signal. If an image of an optically black stripe is viewed against a light background as in figure 26, then the waveform trace of a single horizontal line is as shown in figure 27. The trace was acquired with a digitizing oscilloscope designed for tv waveform analysis. The voltage within the dark band region should correspond to residual photons scattered into this region of the image and might be expected to drop when the lens cap is put on which ensures the absence of light. Instead, the cameras overall signal current changes and the dc level jumps up significantly. If suitably *restored* by shifting the sync tips into coincidence, then the no photon case does jump to the dashed line as shown in the figure. Frame grabbers typically restore the dc level based upon the *porch* regions of the sync information.

This implies that strong irradiance in one region of the sensor could influence the signal in another based on the limiting circuitry of the camera. An experiment was conducted to look for these *non-local* effects. Measurements were made on the analog waveforms recorded by oscilloscope to eliminate uncontrollable variables involved with the frame grabber. The optical layout is sketched in figure 28. An arc source was collimated and used to directly illuminate half of the video sensor and a temperature stabilized blackbody cavity was imaged onto the other half. The intensity of the arc source was adjusted by inserting Wratten gelatin filters into the beam. The camera lens was removed from the camera head to avoid photon scatter from optics proximate to the sensor. A blackbody cavity was used as a source so that scattered light from the room would not affect the radiance of the object since by definition this is governed by cavity temperature alone. Figure 29 shows a plot of measured voltages as a function of the neutral density filter label. As is well known *neutral* is used somewhat euphemistically as shown by the partial spectrophotometer trace [See figure 30.] of the 0.3 filter used. The transmission is changing rapidly in the region where the CCD sensor is becoming more sensitive. Several troubling features will be obvious to the reader. For example when the first attenuation filter is introduced, the analog output response rises! The camera was obviously being driven to nonlinearity in this region. Even in reasonably exposed regions, the mV signal did not drop by three orders of magnitude as would occur if the filter labels were taken literally. It is encouraging that the relative blackbody irradiance varied by less than 2% which might very well be determined by the experimental design.

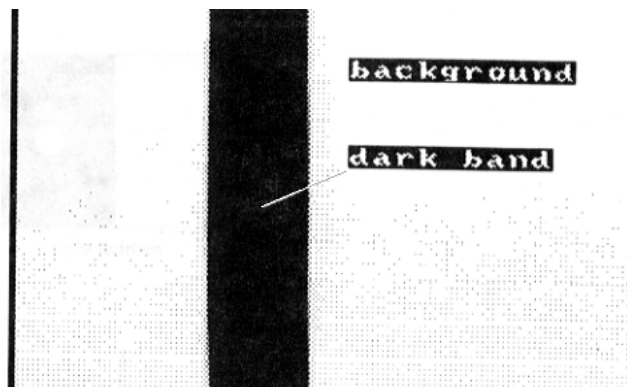


Figure 26. Dc shift example image.

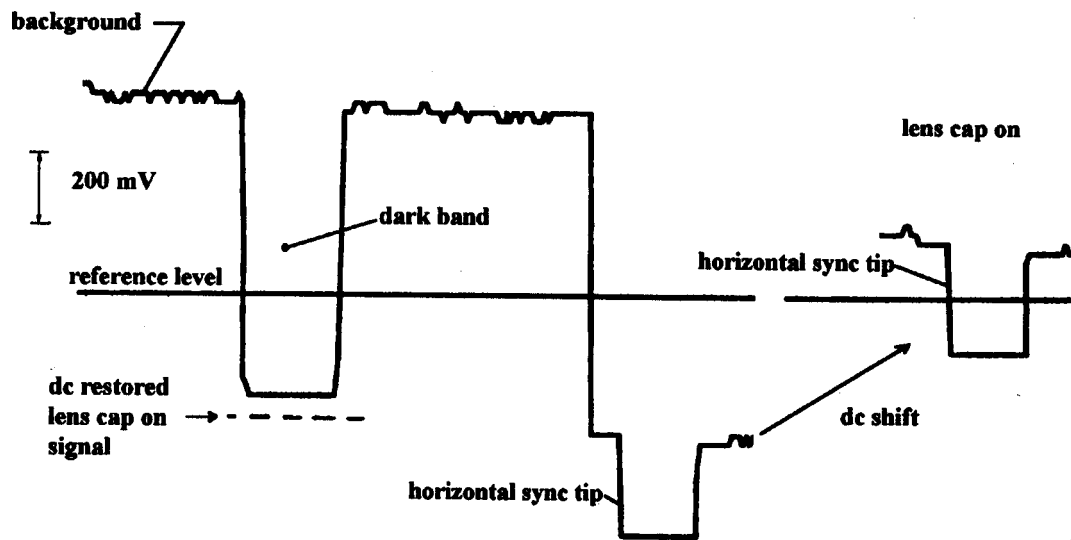


Figure 27. Single horizontal line of image in figure 26.

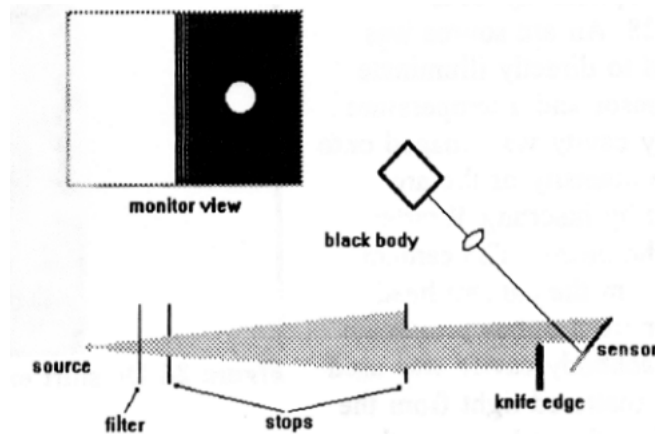


Figure 28. Experimental setup to test for non local irradiance effects.

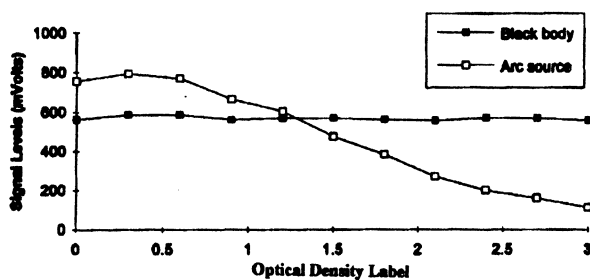


Figure 29. Local blackbody radiance as non local irradiance is varied.

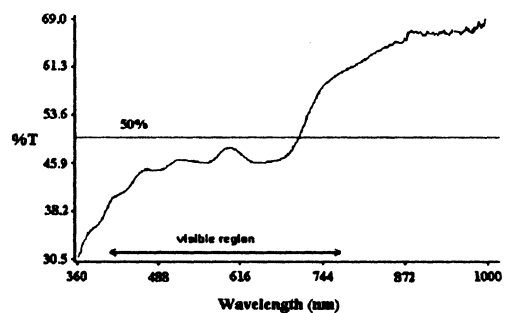


Figure 30. Typical *neutral* density filter wavelength dependence.

6. CONCLUSIONS

Commercial solid state cameras are being used in a variety of field applications for quantitative measurement purposes. The user is well advised to recall that these are analog devices designed for viewing and not targeted to the scientific community as are their slow scan cousins. Much of the

control circuitry designed into the cameras are not under user control. The problem is further compounded by strategies built into frame grabber design. In short there are a number of arbitrary *settings* between the irradiance on the focal plane array and the PC representation.

A number of powerful analytical tools are available from the photogrammetry community to calibrate optical and affinity distortions for videometry applications. Irradiance and frame registration calibrations are more difficult still and will be ameliorated as video rate digital cameras become available.

Acknowledgement

The authors gratefully acknowledge the assistance of Stephen B. Jones for design and construction of the low budget calibration device.

REFERENCES

1. Snow, W.L., Burner, A.W., Goad, W.K., and Gray, D.L.: Video Model Deformation (VMD) System and Stereo Electra Optical Tracking System (SETS) in NASA CP 3010 Second Workshop on Cryogenic Wind-Tunnel Models Design and Fabrication, Hampton, Va. November 3-5, 1987.
2. Burner, A.W., Snow, W.L., Goad, W.K., and Childers, B.A.: A Digital Video Model Deformation System, Proceedings of the ICIASF Record, *International Congress on Instrumentation in Aerospace Simulation Facilities*, Williamsburg, Va. June 22—25, 1987.
3. Bilanin, Alan J.; Teske, Milton E.; and Curtiss, Howard C., Jr.: Feasibility of an Onboard Wake Vortex Avoidance System. C.D.I. Report No. 87-02 Continuum Dynamics Inc. P.O. Box 3073, Princeton, New Jersey, 08543. April, 1987.
4. Childers, Brooks A., and Snow, Walter L.: Video Photographic Considerations for Measuring the Proximity of a Probe Aircraft with a Smoke Seeded Trailing Vortex. NASA TM 102691, June 1990.
5. Snow, Walter L.; Childers, Brooks A., Jones, Stephen B., and Fremaux, Charles M.: Recent experience with implementing a video based six—degree—of—freedom measurement system for airplane models in a 20 foot diameter vertical spin tunnel. SPIE Proceedings Volume 1820, Videometrics, February, 1992.
6. A.M. Skow, and G. E. Erickson, “Modern Fighter Aircraft Design for High-Angle-of-Attack Maneuvering”, pp. 4-1 to 4-59, in AGARD Lecture Series No. 121 entitled High Angle-of-Attack Aerodynamics, published December 1982.
7. Lamar, John E., Brown, Philip W., Bruce, Robert A., Pride, Joseph D. Jr., Smith, Ronald H., and Johnson, Thomas D., Jr., Operational Performance of Vapor-Screen Systems for In-Flight Visualization of Leading-Edge Vortices in the F-106B Aircraft. NASA TM-4004, Sept. 1987.
8. Lamar, John E., and Johnson, Thomas D., Jr.: Sensitivity of F-106B Leading-Edge-Vortex Images to Flight and Vapor-Screen Parameters, NASA TP-2818, June, 1988.
9. Washburn, Anthony E., Jenkins, Luther N., and Ferman, Marty, A.: Experimental Investigations of Vortex-Fin Interaction, AIAA paper no. 93-0050, *31st Aerospace Sciences Meeting and Exhibit*, January 11-14, 1993, Reno, NV.

10. H. M. Karara, Editor in Chief, *Non-Topographic Photogrammetry*, 2nd Edition 1989, American Society for Photogrammetry and Remote Sensing, Falls Church, Virginia.
11. Geometric Software, 17 Toxteth Park Street, Coburg 3058, Australia.
12. Horst, A. Beyer, "Advances in Characterization and Calibration of Digital Imaging Systems", pp 545-555, *International Archives of Photogrammetry and Remote Sensing*, Volume XXIX, Part B5, Commission V. 1992.
13. Smith, Warren J.: *Modern Optical Engineering*, second edition, New York, McGraw-Hill, Inc., 1990.
14. Fraser, C.S.: Refraction Considerations for Photogrammetric Measurements in a Thermal Vacuum Chamber, *Photogrammetric Record*, Volume 14, No. 79, pp. 99-112.
15. W.E. Johnston, D. Robertson, and B. L. Tierney: "Acquisition of Digital Images from Video Tape", pp 273-282, *Pattern Recognition and Image Processing in Physics. Proceedings of the Thirty-Seventh Scottish Universities Summer School in Physics*. Ed. R. A. Vaughan, Adam-Huger Bristol, U.K. 1991.
16. Fraser, C. S.: Photogrammetric Measurement to One Part in a Million. *Photogrammetric Engineering and Remote Sensing*, 58(3) pp. 305-310, 1992.
17. Trinder, J.C.: Precision of Digital Target Location, *Photogrammetric Engineering and Remote Sensing*, Vol. 55, No. 6, June 1989, pp. 883-886.
18. McLean Ian S. : *Electronic and Computer-aided Astronomy: From Eyes to Electronic Sensors*, Halsted Press, a division of John Wiley & Sons, New York, 1989.